INTERNATIONAL JOURNAL FOR NUMERICAL AND ANALYTICAL METHODS IN GEOMECHANICS
Int. J. Numer. Anal. Meth. Geomech. 2011; **35**:761–786
Published online 20 April 2010 in Wiley Online Library (wileyonlinelibrary.com). DOI: 10.1002/nag.919

Dynamic responses of a poroelastic half-space from moving trains caused by vertical track irregularities

Z. G. Cao, Y. Q. Cai, H. L. Sun*, † and C. J. Xu

MOE Key Laboratory of Soft Soils and Geoenvironmental Engineering, Zhejiang University, Hangzhou 310027, People's Republic of China

SUMMARY

The vibrations of railway tracks on a poroelastic half-space generated by moving trains are investigated through a vehicle–track–ground coupling model. The theoretical model incorporates a vehicle, a track, and a fully saturated poroelastic half-space soil medium. The source of vibration excitation is divided into two components: the quasi-static loads and the dynamic loads. The quasi-static loads are related to the static component of the axle loads, whereas the dynamic loads are due to the dynamic wheel–rail interaction. A linear Hertizian contact spring is introduced between each wheelset and the rail to consider the dynamic loads. Biot's dynamic theory is used to characterize the poroelastic half-space soil medium. Using the Fourier transform, the governing equations for the track–ground system are solved and the numerical results are presented for a single axle vehicle model. The different dynamic characteristics of the elastic soil medium and the saturated poroelastic medium are investigated. In addition, the different roles of the moving axle loads and the roughness-induced dynamic loads are identified. It is concluded that the vibration level of the free field off the track predicted by the poroelastic soil medium is smaller than that predicted by the elastic soil medium for vehicle speed below the Rayleigh wave speed of the poroelastic half-space, whereas it is larger for vehicle speed above the Rayleigh wave speed. The dynamic loads play an important role in the dynamic responses of the track–ground system. Copyright © 2010 John Wiley & Sons, Ltd.

Received 5 August 2009; Revised 2 December 2009; Accepted 23 February 2010

KEY WORDS: vehicle–track–ground coupling; Biot's theory; poroelasticity; moving train; rail irregularity

1. INTRODUCTION

The consequences of railway traffic, in terms of environmental polluters, have become more important in view of the fact that the speed of trains has elevated rapidly. A number of theoretical models have been reported to predict the train-induced ground vibration. Krylov [1] proposed a model for the prediction of the levels of the track vibration generated by a superfast train. Treating the ground as an elastic half-space, an approximate expression for Green's function of the elastic half-space was used, by taking only the Rayleigh wave's contribution into account. It was shown that a very large increase in the vibration level might occur if the train's speed exceeded the velocity of Rayleigh waves in the ground. Later, Vostroukhov and Metrikine [2] and Takemiya and Bian [3] investigated the dynamic responses of the track–ground system generated by trains moving at

*Correspondence to: H. L. Sun, MOE Key Laboratory of Soft Soils and Geoenvironmental Engineering, Zhejiang University, Hangzhou 310027, People's Republic of China.
†E-mail: honglei.s@gmail.com

Contract/grant sponsor: National Natural Science Foundation of China; contract/grant number: 50778136
Contract/grant sponsor: Provincial Natural Science Foundation of Zhejiang; contract/grant number: R1080819
Contract/grant sponsor: China Postdoctoral Science Foundation; contract/grant number: 20090450182

different speeds by use of models of a Euler beam discretely supported by sleepers on the elastic or visco-elastic soil medium. Sheng and Jones [4] and Picoux and Le Houédec [5] studied the ground vibration generated by train loads through a sandwich beam-structure track model consisting of rail track, continuous sleeper, and the ballast, and the soil medium was modeled as a layered elastic half-space. On the basis of Sheng and Jones [4], Cai *et al.* [6] extended the research of the dynamic response of the track–ground system by using a saturated poroelastic soil model. The effects of the poroelasticity of soil on the vibration of the track–ground system were studied. For these models above, the train loads were treated as a series of constant loads (axle load). However, during the passage of the train, the dynamic load can be generated due to the rail irregularities and the wheel flats. It is known that, in some circumstances, the dynamic loads have an apparent effect on the velocity and acceleration responses of the rail track and the free-field of the ground surface. In fact, it was found in Lai *et al.* [7] as well as Sheng *et al.* [8] that the consideration of only quasi-static axle loads would underestimate the actual vibration response level generally, especially for high excitation frequency.

To calculate the vertical dynamic wheel–rail forces, a vehicle dynamics model must be adopted. Recently, several vehicle dynamics models have been developed, such as Zai and Cai [9] and Sun and Dhanasekar [10]. The aim of such models was to analyze the ride quality, the hunting motion etc., rather than the ground vibration. In these models, the ground was treated as a rigid or Winkler foundation and the track is often truncated into a finite length. As a result, these models were not able to consider the wave propagation in the rail beam. Meanwhile, these models could not investigate the train-induced ground vibration as well. Sheng *et al.* [8] proposed a vehicle–track–ground coupling model consisting of a vehicle, an infinite track, and an elastic half-space. A linear Hertzian contact spring [11] was introduced between each wheelset and the rail to calculate the dynamic loads. In their work, the vibration velocity spectra were presented for the quasi-static induced levels and the total levels, respectively, and it was concluded that the dynamic loads played an important role in the analysis of the ground vibration. However, the ground was modeled as elastic soil medium and no time-domain results for the ground vibration were presented by them.

For simplicity, the soil medium is generally modeled as an elastic or visco-elastic medium in many researches. However, underground water often exists in the soil medium. The soil medium is actually a two-phase medium. Biot [12, 13] pioneered the development of an elastodynamic theory for a fluid-filled elastic porous medium. By applying Biot's theory, Siddharthan *et al.* [14] studied the dynamic response of a layered poroelastic half-space subjected to the moving loads, and the dynamic fundamental equations are solved approximately, neglecting the coupling between the soil skeleton and the fluid. On the basis of Siddharthan *et al.* [14], Theodorakopoulos [15], Theodorakopoulos and Chassiakoos [16] obtained the steady-state dynamic response of the poroelastic soil subjected to a line load under plane strain conditions with the relative motion between the solid and fluid phases. Recently, Lu and Jeng [17], Jin [18] and Cai *et al.* [6] investigated the dynamic response of a poroelastic half-space soil medium subjected to the moving loads in the three-dimensional condition. The results confirmed that the dynamic properties of the poroelastic soil medium were different from those of the elastic, especially when the train speed approaches the Rayleigh wave speed of the half-space. But in their work, the dynamic forces resulting from the irregularities between the wheels and rails were not considered at all, which may be of significance. Therefore, a fully saturated poroelastic soil model is required to investigate the ground vibrations from moving trains considering the dynamic wheel–rail forces resulting from the vertical track irregularities.

The present work is an extension of Cai *et al.* [6] considering the contribution of the dynamic wheel–rail forces resulting from the rail irregularities for the ground vibrations. The theoretical model is proposed, incorporating a vehicle, a track, and a fully saturated poroelastic half-space soil medium. This model uses both the moving axle loads and the rail irregularities as the inputs. The rail irregularities are assumed to have a sinusoidal profile. It is also assumed that the wheelsets are always in contact with the rails. Compatibility of the displacements at wheel–rail contact points couples the vehicles and the track–ground subsystem, and yields the equations for the dynamic wheel–rail loads. Biot's dynamic theory is used to characterize the poroelastic half-space soil

DOI: 10.1002/nag

medium. The governing equations of the track–ground system are solved by the Fourier transform. The time-domain results are obtained by the fast Fourier transform (FFT). The effects of the rail bending stiffness on the dynamic response levels are studied for vehicle speeds below, and above the Rayleigh wave speed of the half-space. The different characteristics of the elastic soil medium and the saturated poroelastic medium subjected to the moving train loads are studied. In addition, the different roles of the moving axle loads and the roughness-induced dynamic loads to the track–ground vibration are identified for various speeds.

2. GOVERNING EQUATIONS OF THE VEHICLE AND TRACK–GROUND SYSTEM

2.1. Receptances of the vehicle at the wheelsets

The receptance herein denotes the displacement amplitude of the wheelsets due to a unit vertical harmonic load with an excitation frequency Ω. The vehicle model used in Sheng *et al.* [8] is introduced. As shown in Figure 1, the vehicles are represented as multiple rigid body systems and the vertical dynamics of the vehicles are coupled to the track–ground model by introducing linear Hertzian contact springs [11] between each wheelset and the rails. The differential equation of motion for a single vehicle is given by

$$\mathbf{M_V}\ddot{\mathbf{Z}}_\mathbf{V}(t)+\mathbf{K_V}\mathbf{Z_V}(t)=-\mathbf{BP}(t) \tag{1}$$

where $\mathbf{M_V}$ and $\mathbf{K_V}$ denote the mass and stiffness matrices of the vehicle, respectively, $\mathbf{Z_V}(t)$ denotes the displacement vector, $\mathbf{P}(t)$ denotes the wheel–rail force vector, and $\mathbf{B}$ is a matrix of unit and zero elements (see Appendix A).

The roughness-induced dynamic loads between the wheel–rail are harmonic loads with angular frequency Ω, where $\Omega=2\pi c/\lambda_1$, λ_1 is the wavelength of the rail profile and c is the vehicle

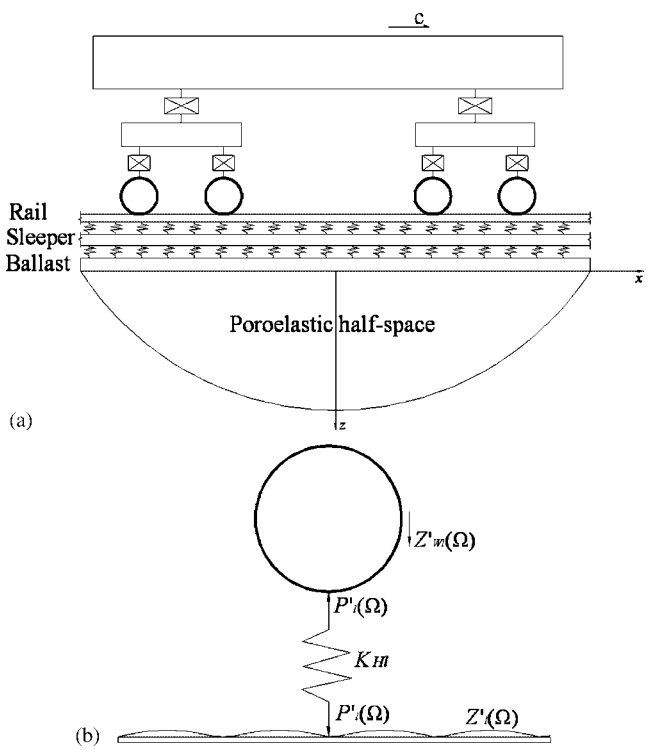

Figure 1. Model of the vehicle–track–ground coupling system: (a) the vehicle–track–ground system and (b) coupling of the lth wheelset with the rails.

DOI: 10.1002/nag

speed. As shown by Sheng *et al.* [8], $\mathbf{P}(t)$ and $\mathbf{Z_V}(t)$ can be expressed as: $\mathbf{P}(t)=\mathbf{P}'(\Omega)e^{i\Omega t}$ and $\mathbf{Z_V}(t)=\mathbf{Z}'_{\mathbf{V}}(\Omega)e^{i\Omega t}$. Then Equation (1) can be written into

$$\mathbf{Z}'_{\mathbf{V}}(\Omega)=-(\mathbf{K_V}-\Omega^2\mathbf{M_V})^{-1}\mathbf{B}\mathbf{P}'(\Omega) \tag{2}$$

The receptance between the jth and kth wheelsets within a vehicle is denoted by Δ^{W}_{jk}('W' means wheelset), where $j, k=1,2,\ldots,N$; N is the number of wheelsets of the vehicle. Δ^{W}_{jk} denotes the displacement amplitude of the jth wheelset due to a unit vertical harmonic load with an excitation frequency Ω exerted at the kth wheelset. The displacement vector of the wheelset in the vehicle is expressed as

$$\mathbf{Z}'_{\mathbf{W}}(\Omega)=(Z'_{\mathrm{W}1}(\Omega), Z'_{\mathrm{W}2}(\Omega), Z'_{\mathrm{W}3}(\Omega), ..., Z'_{\mathrm{W}N}(\Omega))^{\mathrm{T}} \tag{3}$$

and

$$\mathbf{P}'(\Omega)=(P'_1(\Omega), P'_2(\Omega), P'_3(\Omega), ..., P'_N(\Omega))^{\mathrm{T}} \tag{4}$$

is the wheel–rail force vector for a vehicle.

The displacement vector of the wheelsets is part of that for the corresponding vehicle. Therefore, it can be written as

$$\mathbf{Z}'_{\mathbf{W}}(\Omega)=\mathbf{A}\mathbf{Z}'_V(\Omega) \tag{5}$$

where $\mathbf{A}=\mathbf{B}^{\mathrm{T}}$ (see the Appendix A). Thus

$$\mathbf{Z}'_{\mathbf{W}}(\Omega)=-\mathbf{\Delta^W}\mathbf{P}'(\Omega)=-\mathbf{A}(\mathbf{K_V}-\Omega^2\mathbf{M_V})^{-1}\mathbf{B}\mathbf{P}'(\Omega) \tag{6}$$

$$\mathbf{\Delta^W}=\begin{bmatrix}\Delta^{\mathrm{W}}_{11} & \cdots & \Delta^{\mathrm{W}}_{1N}\\ \vdots & \cdots & \vdots\\ \Delta^{\mathrm{W}}_{N1} & \cdots & \Delta^{\mathrm{W}}_{\mathbf{NN}}\end{bmatrix}=\mathbf{A}(\mathbf{K_V}-\Omega^2\mathbf{M_V})^{-1}\mathbf{B} \tag{7}$$

Equation (7) gives the receptance matrix at the wheelsets for a single vehicle. Suppose there are N_1 identical vehicles being considered, the total number of the wheel–rail loads is $M=N_1N$. The receptance matrix at the wheelsets for the train, denoted by $\mathbf{\Delta^T}$('T' means the train), is given by

$$\mathbf{\Delta^T}=\mathrm{diag}(\mathbf{\Delta^W},\ldots,\mathbf{\Delta^W})=\begin{bmatrix}\mathbf{\Delta^W} & \cdots & 0\\ \vdots & \vdots & \vdots\\ 0 & \cdots & \mathbf{\Delta^W}\end{bmatrix} \tag{8}$$

The elements of matrix $\mathbf{\Delta^T}$ are denoted by Δ^{T}_{lk}, where $k,l=1,2,\ldots,M$.

2.2. *Receptances of the track–ground system at the wheel–rail contact points*

The track model proposed by Picoux and Le Houédec [5] is introduced in this paper. In order to calculate the receptance of the track–ground system, a unit vertical harmonic load $e^{i\Omega t}$ is applied on the rail, which is pointing downwards and located at $x=0$ when $t=0$, moving along the rails at speed c. The governing equation for a rail represented by a Euler beam is written as:

$$EI\frac{\partial^4 u_{\mathrm{R}}(x,t)}{\partial x^4}+m_{\mathrm{R}}\frac{\partial^2 u_{\mathrm{R}}}{\partial t^2}+k_{\mathrm{P}}[u_{\mathrm{R}}(x,t)-u_{\mathrm{S}}(x,t)]=e^{i\Omega t}\delta(x-ct) \tag{9}$$

in which u_{R} is the vertical displacement of the Euler Beam, EI is the bending stiffness of the rail beam, m_{R} is the mass of the rail per unit length, k_{P} denotes the spring constant of the rail pads, and u_{S} is the vertical displacement of the sleepers.

DOI: 10.1002/nag

It is denoted in the literatures [19, 20] that the effect of the discreteness of the rail supports may be neglected when the dominating frequency content of the response is not in the vicinity of the so-called pinned-pinned resonance frequency. This frequency is normally located in the range 700-1000 Hz depending on the rail properties and the sleeper distance. The main frequency range of interest for the perception of ground vibration is about 5–80 Hz, therefore it is suitable to represent the sleepers by a continuous mass:

$$m_S \frac{\partial^2 u_S(x,t)}{\partial t^2} + k_P[u_S(x,t) - u_R(x,t)] = -F_S(x,t) \tag{10}$$

where m_S is the mass of the sleeper per unit length, and F_S is the load between the sleepers and the ballast.

The ballast is first considered by Cosserat model (Suiker *et al.* [21]). At the top and bottom of the ballast, the system can be written as:

$$\frac{m_B}{6}\left[2\frac{\partial^2 u_S(x,t)}{\partial t^2} + \frac{\partial^2 u_B(x,t)}{\partial t^2}\right] + k_B[u_S(x,t) - u_R(x,t)] = F_S(x,t) \tag{11}$$

$$\frac{m_B}{6}\left[\frac{\partial^2 u_S(x,t)}{\partial t^2} + 2\frac{\partial^2 u_B(x,t)}{\partial t^2}\right] + k_B[-u_S(x,t) + u_B(x,t)] = -F_B(x,t) \tag{12}$$

in which m_B is the mass of the ballast per unit length, k_B is the spring constant between ballast and sleepers, F_B is the ballast load on the soil, and u_B is the vertical displacement of the ballast.

Based on the assumption of neglecting the apparent mass density, the linearized dynamic equations of motion for a fully saturated poroelastic are given by Biot [12] as:

$$\mu u_{i,jj} + (\lambda + \alpha^2 M + \mu) u_{j,ji} + \alpha M w_{j,ji} = \rho \ddot{u}_i + \rho_f \ddot{w}_i \tag{13}$$

$$\alpha M u_{j,ji} + M w_{j,ji} = \rho_f \ddot{u}_i + m \ddot{w}_i + b \dot{w}_i \tag{14}$$

where, u_i, w_i ($i = x, y, z$) are the solid displacement components and the fluid displacement related to solid displacement along the x, y, and z directions; dots on u_i and w_i indicate the derivatives with respect to time t; λ and μ are Lamé constants; α and M are Biot's parameters accounting for the compressibility of the two-phased material; $\rho = n\rho_f + (1-n)\rho_s$, where ρ_f and ρ_s are the mass densities of the fluid and solid and n is the porosity; m is a density-like parameter that depends on ρ_f and the geometry of the pores; b is a parameter accounting for the internal friction due to the relative motion between the solid and the pore fluid. The parameter b equals to the ratio between the fluid viscosity and the intrinsic permeability of the medium ($b = 0$ for zero internal friction). The constitutive relations can be expressed as:

$$\sigma_{ij} = \lambda \delta_{ij} \theta + \mu(u_{i,j} + u_{j,i}) - \alpha \delta_{ij} p \tag{15}$$

$$p = -\alpha M \theta + M \varsigma \tag{16}$$

$$\varsigma = -w_{i,i} \tag{17}$$

where $\theta = u_{i,i}$ is solid strain; σ_{ij} is the total stress component of bulk material; p is the pore water pressure.

In this paper, the dimensionless variables are adopted. All the displacements are non-dimensionalized with respect to the unit length a. Pore water pressures and stresses are non-dimensionalized with respect to the shear modulus μ. The load between the rail, sleeper, ballast, and ground are non-dimensionalized with respect to μa^2. All variables are then replaced by the corresponding dimensionless quantities, denoted by a superscript asterisk (*). The dimensionless time is defined as:

$$\tau = (t/a)\sqrt{\mu/\rho} \tag{18}$$

DOI: 10.1002/nag

The following non-dimensional parameters are also defined: $k_{\mathrm{B}}^{*}=k_{\mathrm{B}}/\mu a$, $k_{\mathrm{P}}{}^{*}=k_{\mathrm{P}}/\mu a$, $\mathbf{K}_{\mathbf{V}}^{*}=\mathbf{K}_{\mathbf{V}}/\mu a$, $\mathbf{M}_{\mathbf{V}}^{*}=\mathbf{M}_{\mathbf{V}}/\rho a^{3}$, $\lambda^{*}=\lambda/\mu$, $M^{*}=M/\mu$, $\rho_{\mathrm{f}}^{*}=\rho_{\mathrm{f}}/\rho$, $m^{*}=m/\rho$, $b^{*}=ab/\sqrt{\rho\mu}$, $\beta=EI/\mu a^{2}$, $m_{\mathrm{R}}^{*}=m_{\mathrm{R}}^{*}/\rho a^{2}$, $m_{\mathrm{S}}^{*}=m_{\mathrm{S}}^{*}/\rho a^{2}$, $c_{0}=c/V_{\mathrm{s}}$, V_{s} is the shear wave velocity of the half-space, expressed as $V_{\mathrm{s}}=\sqrt{\mu/\rho_{\mathrm{s}}}$, c is the vehicle speed.

The Fourier transform with respect to dimensionless time τ is defined as

$$\tilde{f}(x^{*},y^{*},z^{*},\omega)=\int_{-\infty}^{\infty}f(x^{*},y^{*},z^{*},\tau)\mathrm{e}^{-i\omega\tau}\,\mathrm{d}\tau \tag{19}$$

and the inverse relationship is given by

$$f(x^{*},y^{*},z^{*},\tau)=\frac{1}{2\pi}\int_{-\infty}^{\infty}\tilde{f}(x^{*},y^{*},z^{*},\omega)\mathrm{e}^{i\omega\tau}\,\mathrm{d}\omega \tag{20}$$

By use of Equations (19) and after some manipulations, Equations (13)–(17) lead to the following forms:

$$\nabla^{2}\tilde{u}_{x}+(\lambda^{*}+1)\frac{\partial\tilde{\theta}}{\partial x}+\Omega^{2}(1-\rho^{*}\vartheta)\tilde{u}_{x}-(\alpha-\vartheta)\frac{\partial\tilde{p}}{\partial x}=0 \tag{21}$$

$$\nabla^{2}\tilde{u}_{y}+(\lambda^{*}+1)\frac{\partial\tilde{\theta}}{\partial y}+\Omega^{2}(1-\rho^{*}\vartheta)\tilde{u}_{y}-(\alpha-\vartheta)\frac{\partial\tilde{p}}{\partial y}=0 \tag{22}$$

$$\nabla^{2}\tilde{u}_{z}+(\lambda^{*}+1)\frac{\partial\tilde{\theta}}{\partial z}+\Omega^{2}(1-\rho^{*}\vartheta)\tilde{u}_{z}-(\alpha-\vartheta)\frac{\partial\tilde{p}}{\partial z}=0 \tag{23}$$

$$\nabla^{2}\tilde{p}+\frac{\rho^{*}\Omega^{2}}{M^{*}\vartheta}\tilde{p}+\frac{\rho^{*}\Omega^{2}(\alpha-\vartheta)}{\vartheta}\tilde{\theta}=0 \tag{24}$$

in which $\vartheta=\rho^{*}\omega^{2}/(m^{*}\omega^{2}-ib^{*}\omega)$.

From Equations (21)–(24), the following equation can be obtained:

$$\nabla^{4}\tilde{p}+a_{1}\nabla^{2}\tilde{p}+a_{2}\tilde{p}=0 \tag{25}$$

where

$$a_{1}=\frac{(m^{*}\omega^{2}-ib^{*}\omega)(\lambda^{*}+\alpha^{2}M^{*}+2)+M^{*}\omega^{2}-2\alpha M^{*}\rho^{*}\omega^{2}}{(\lambda^{*}+2)M^{*}} \tag{26}$$

$$a_{2}=\frac{(m^{*}\omega-ib^{*})\omega^{3}-(\rho^{*})^{2}\omega^{4}}{(\lambda^{*}+2)M^{*}} \tag{27}$$

The Fourier transforms with respect to x^{*} and y^{*} is defined as

$$\bar{\bar{\tilde{f}}}(\xi,\eta,z^{*},\omega)=\int_{-\infty}^{\infty}\int_{-\infty}^{\infty}\tilde{f}(x^{*},y^{*},z^{*},\omega)\mathrm{e}^{-i(\xi x^{*}+\eta y^{*})}\,\mathrm{d}x^{*}\,\mathrm{d}y^{*} \tag{28}$$

and the inverse relationship is given by

$$\tilde{f}(x^{*},y^{*},z^{*},\omega)=\frac{1}{4\pi^{2}}\int_{-\infty}^{\infty}\int_{-\infty}^{\infty}\bar{\bar{\tilde{f}}}(\xi,\eta,z^{*},\omega)\mathrm{e}^{i(\xi x^{*}+\eta y^{*})}\,\mathrm{d}\xi\,\mathrm{d}\eta \tag{29}$$

The application of Fourier integral transforms to Equations (15), (16) and (21)–(25) leads to:

$$\bar{\bar{\tilde{p}}}(\xi,\eta,z^{*},\omega)=A(\xi,\eta,\omega)\mathrm{e}^{-\gamma_{1}z^{*}}+B(\xi,\eta,\omega)\mathrm{e}^{-\gamma_{2}z^{*}} \tag{30}$$

$$\bar{\bar{\tilde{u}}}_{z}(\xi,\eta,z^{*},\omega)=\gamma_{1}F_{1}A(\xi,\eta,\omega)\mathrm{e}^{-\gamma_{1}z^{*}}+\gamma_{2}F_{2}B(\xi,\eta,\omega)\mathrm{e}^{-\gamma_{2}z^{*}}+C(\xi,\eta,\omega)\mathrm{e}^{-\gamma_{3}z^{*}} \tag{31}$$

DOI: 10.1002/nag

$$\bar{\bar{\tilde{u}}}_y(\xi,\eta,z^*,\omega) = -i\eta[F_1 A(\xi,\eta,\omega)\mathrm{e}^{-\gamma_1 z^*} + F_2 B(\xi,\eta,\omega)\mathrm{e}^{-\gamma_2 z^*}] + i D(\xi,\eta,\omega)\mathrm{e}^{-\gamma_3 z^*} \tag{32}$$

$$\bar{\bar{\tilde{u}}}_x(\xi,\eta,z^*,\omega) = -\frac{i}{\xi}\{[E_1 + (\xi^2 - b_1^2)F_1]A\mathrm{e}^{-\gamma_1 z^*} + [E_2 + (\xi^2 - b_2^2)F_2]B\mathrm{e}^{-\gamma_2 z^*} + (C\gamma_3 + D\eta)\mathrm{e}^{-\gamma_3 z^*}\} \tag{33}$$

where

$$\gamma_i = \sqrt{\xi^2 + \eta^2 - L_i^2}, \quad i = 1, 2, \quad \gamma_3 = \sqrt{\xi^2 + \eta^2 - S^2},$$

$$E_i = \frac{\vartheta M^* b_i^2 - \rho^* \omega^2}{\rho^* \omega^2 (\alpha - \vartheta) M^*}, \quad i = 1, 2, \quad F_i = \frac{\lambda^* E_i + E_i - \alpha + \vartheta}{S^2 - b_i^2},$$

$$b_1^2 = \frac{a_1 + \sqrt{a_1^2 - 4a_2}}{2}, \quad b_2^2 = \frac{a_1 - \sqrt{a_1^2 - 4a_2}}{2},$$

$$S^2 = (1 - \rho^* \vartheta)\omega^2$$

As the model studied concerns the half-space problem, the real part of γ_i ($i = 1, 2, 3$) must be positive to satisfy the infinite boundary conditions of the half-space.

The boundary conditions of the half-space are given as follows:

$$\tau_{xz}(x^*, y^*, 0, \tau) = 0 \tag{34}$$

$$\sigma_{zz}(x^*, y^*, 0, \tau) = -\frac{1}{2a}\Pi(y^*) F_{\mathrm{B}}^*(x^*, \tau) \tag{35}$$

$$\tau_{yz}(x^*, y^*, 0, \tau) = 0 \tag{36}$$

$$p(x^*, y^*, 0, \tau) = 0 \tag{37}$$

$$u_z(x^*, 0, 0, \tau) = u_{\mathrm{B}}(x^*, \tau) \tag{38}$$

The load distributing function is defined as:

$$\Pi(y) = \begin{cases} 1 & |y| \leqslant L_{\mathrm{Bal}}^* \\ 0 & |y| > L_{\mathrm{Bal}}^* \end{cases} \tag{39}$$

From Equations (34)–(37), the following equation can be obtained:

$$\bar{\bar{\tilde{u}}}_z(\xi,\eta,z^*,\omega) = -\frac{\bar{\Pi}(\eta)}{2L_{\mathrm{Bal}}^*}\bar{\tilde{F}}_{\mathrm{B}}^*(\xi,\omega)\phi(\xi,\eta,z^*,\omega) \tag{40}$$

where

$$\phi(\xi,\eta,z^*,\Omega) = \frac{1}{\Gamma}[(\gamma_3^2 + \xi^2 + \eta^2)(\gamma_2 a_2 \mathrm{e}^{-\gamma_2 z^*} - \gamma_1 a_1 \mathrm{e}^{-\gamma_1 z^*}) + (\gamma_1 g_5 - \gamma_2 g_6)\mathrm{e}^{-\gamma_3 z^*}]$$

$$g_i = E_i + (2\xi^2 - b_i^2)F_i, \quad i = 1, 2$$

$$g_3 = \lambda^* E_1 - 2\gamma_1^2 F_1 - \alpha, \quad g_4 = \lambda^* E_2 - 2\gamma_2^2 F_2 - \alpha$$

$$g_5 = g_1 + 2\eta^2 F_1, \quad g_6 = g_2 + 2\eta^2 F_2$$

$$\Gamma = (g_4 - g_3)(\gamma_3^2 + \xi^2 + \eta^2) - 2\gamma_3(\gamma_1 g_5 - \gamma_2 g_6)$$

In Equation (40), $\bar{\tilde{F}}_{\mathrm{B}}(\xi,\omega)$ remains unknown and can be resolved by the following equations.

DOI: 10.1002/nag

Applying Fourier transform with respect to x^* and τ for Equations (9)–(12) and (38), the following dimensionless equations can be obtained by eliminating $F_S^*(\xi,\omega)$:

$$\alpha_1(\xi,\omega)\bar{\tilde{u}}_R(\xi,\omega)-k_P^*\bar{\tilde{u}}_S(\xi,\omega)=\alpha_2(\xi,\omega) \tag{41}$$

$$-k_P^*\bar{\tilde{u}}_R(\xi,\omega)+\alpha_3(\xi,\omega)\bar{\tilde{u}}_S(\xi,\omega)+\alpha_4(\xi,\omega)\bar{\tilde{u}}_B(\xi,\omega)=0 \tag{42}$$

$$\alpha_4(\xi,\omega)\bar{\tilde{u}}_S(\xi,\omega)+\alpha_5(\xi,\omega)\bar{\tilde{u}}_B(\xi,\omega)=-\bar{\tilde{F}}_B^*(\xi,\omega) \tag{43}$$

$$\bar{\tilde{u}}_B(\xi,\omega)=\alpha_6(\xi,\omega)\bar{\tilde{F}}_B^*(\xi,\omega) \tag{44}$$

where

$$\alpha_1(\xi,\omega)=\delta\xi^4-m_R^*\omega^2+k_P^*,\quad \alpha_2(\xi,\omega)=2\pi\delta(\omega+\xi c_0-\Omega),$$

$$\alpha_3(\xi,\omega)=-m_B^*\omega^2/2+k_P^*+k_B^*-m_S^*\omega^2,\quad \alpha_4(\xi,\omega)=-m_B^*\omega^2/6-k_B^*,$$

$$\alpha_5(\xi,\omega)=-m_B^*\omega^2/3+k_B^*,\quad \alpha_6(\xi,\omega)=\Psi(\xi,0,\omega),$$

$$\Psi(\xi,0,\omega)=\frac{1}{2\pi}\int_{-\infty}^{\infty}-\bar{\Pi}(\eta)\phi(\xi,\eta,0,\omega)e^{i\eta y}\,dy.$$

By use of Equations (41)–(44), $\bar{\tilde{F}}_B(\xi,\omega)$ is obtained:

$$\bar{\tilde{F}}_B^*(\xi,\omega)=\frac{\alpha_2(\xi,\omega)\alpha_4(\xi,\omega)k_P^*}{\alpha_1(\xi,\omega)\alpha_6(\xi,\omega)\alpha_4^2(\xi,\omega)-(\alpha_3(\xi,\omega)\alpha_1(\xi,\omega)-k_P^{*2})(1+\alpha_5(\xi,\omega)\alpha_6(\xi,\omega))} \tag{45}$$

Thus, the rail displacement in Fourier transform domain is finally given by:

$$\bar{\tilde{u}}_R^*(\xi,\omega)=\frac{-(\alpha_2(\xi,\omega)\alpha_4(\xi,\omega)^2-\alpha_2(\xi,\omega)\alpha_3(\xi,\omega)\alpha_5(\xi,\omega)-\alpha_4(\xi,\omega)\bar{\tilde{F}}_B^*(\xi,\omega)k_p^*)}{(\alpha_1(\xi,\omega)\alpha_4(\xi,\omega)^2-\alpha_1(\xi,\omega)\alpha_3(\xi,\omega)\alpha_5(\xi,\omega)+\alpha_5(\xi,\omega)k_p^{*2})} \tag{46}$$

The displacement of the rail and ground in the time domain can be expressed as follows by introducing an auxiliary spatial coordinate $x_t^*=x^*-c_0\tau$, and the time-domain results are obtained by the FFT algorithm.

$$u_R^*(x^*,\tau)=\frac{1}{2\pi}\int_{-\infty}^{\infty}\bar{\tilde{u}}_R^*(\xi,\Omega^*-\xi c_0)e^{i\xi x_t^*}\,d\xi\cdot e^{i\Omega^*\tau} \tag{47}$$

$$u_z^*(x^*,y^*,z^*,\tau)=\frac{1}{4\pi^2}\int_{-\infty}^{\infty}\int_{-\infty}^{\infty}\bar{\bar{\tilde{u}}}_z^*(\xi,\eta,\Omega^*-\xi c_0)e^{i\eta y^*}e^{i\xi x_t^*}\,d\eta\,d\xi\cdot e^{i\Omega^*\tau} \tag{48}$$

Equations (47) and (48) can also be expressed as:

$$u_R^*(x^*,\tau)=u_R^{\Omega}(x_t^*)\cdot e^{i\Omega^*\tau} \tag{49}$$

$$u_z^*(x^*,y^*,z^*,\tau)=u_z^{\Omega}(x_t^*,y^*,z^*)\cdot e^{i\Omega^*\tau} \tag{50}$$

Equations (49) and (50) denote that in the auxiliary spatial coordinate, the displacements of the track–ground system are harmonic and have the same vibration frequency as the dynamic load. Thus, the receptance at the jth wheel–rail contact point due to a unit load at the kth wheel–rail contact point on the rail is determined by

$$\Delta_{jk}^R=u_R^{\Omega}(l_{jk}^*) \tag{51}$$

where

$$l_{jk}^*=a_j^*-a_k^* \tag{52}$$

is the dimensionless distance between the two contact points.

DOI: 10.1002/nag

The complex amplitudes of the displacements at the wheel–rail contact points on the rails are given by

$$\mathbf{z}_{\mathrm{R}}'^{*}(\Omega^{*})=\mathbf{\Delta}^{\mathbf{R}}\mathbf{P}'^{*}(\Omega^{*}) \tag{53}$$

where

$$\mathbf{\Delta}^{\mathbf{R}}=\begin{bmatrix} \Delta_{11}^{\mathrm{R}} & \Delta_{12}^{\mathrm{R}} & \cdots & \Delta_{1M}^{\mathrm{R}} \\ \Delta_{21}^{\mathrm{R}} & \Delta_{22}^{\mathrm{R}} & \cdots & \Delta_{2M}^{\mathrm{R}} \\ \vdots & \vdots & \vdots & \vdots \\ \Delta_{M1}^{\mathrm{R}} & \Delta_{M2}^{\mathrm{R}} & \cdots & \Delta_{MM}^{\mathrm{R}} \end{bmatrix} \tag{54}$$

The receptance matrix is non-symmetric due to the load motion.

$$\mathbf{z}_{\mathrm{R}}'^{*}(\Omega^{*})=(z_{\mathrm{R}1}'^{*}(\Omega^{*}), z_{\mathrm{R}2}'^{*}(\Omega^{*}), z_{\mathrm{R}3}'^{*}(\Omega^{*}), \ldots, z_{\mathrm{R}M}'^{*}(\Omega^{*}))^{\mathrm{T}} \tag{55}$$

Equation (55) represents the displacement vector of the rail at the wheel–rail contact points observed in the auxiliary spatial coordinate.

2.3. Coupling of the vehicles and the track–ground system

The rail irregularities are presented by a sinusoidal profile of amplitude A. The profile of the rail irregularities is given by

$$z(x)=A\mathrm{e}^{i(2\pi/\lambda_1)x} \tag{56}$$

where λ_1 denotes the wavelength. The process is assumed to be linear, so that a displacement input is generated at the excitation frequency $f=c/\lambda_1$. The angular frequency is obtained by $\Omega=2\pi c/\lambda_1$. At time t, the lth wheelset arrives at $x=a_l+ct$, thus the displacement input of the rail profile at the lth wheel–rail contact point is

$$z_l(t)=z_l'(\Omega)\mathrm{e}^{i\Omega t}=A\mathrm{e}^{i(2\pi/\lambda_1)(a_l+ct)}=A\mathrm{e}^{i(2\pi/\lambda_1)a_l}\mathrm{e}^{i\Omega t} \tag{57}$$

The coupling of a wheelset with rail is illustrated in Figure 1(b), where $z_{Wl}'(\Omega)\mathrm{e}^{i\Omega t}$ denotes the displacement of the lth wheelset. The wheel and rail deform locally according to the Hertz theory under the action of the contact force. Thus the wheel and rail are coupled by a 'Hertz spring'. Provided that the dynamic contact force is a small fraction of the axle load, the Hertz spring can be taken to be linear. The stiffness of the Hertzian contact spring is denoted by $k_{\mathrm{H}l}$. It is also assumed that the wheelset is always in contact with the rail, thus

$$z_{\mathrm{W}l}'(\Omega)=z_{\mathrm{R}l}'(\Omega)+z_l'(\Omega)+P'(\Omega)/k_{\mathrm{H}l} \tag{58}$$

From Equations (6) and (53), the following relations can be derived

$$z_{\mathrm{W}l}'(\Omega)=-\sum_{k=1}^{M}\Delta_{lk}^{\mathrm{T}}P_k'(\Omega) \tag{59}$$

$$z_{\mathrm{R}l}'(\Omega)=\sum_{k=1}^{M}\Delta_{lk}^{\mathrm{R}}P_k'(\Omega) \tag{60}$$

By non-dimensionalizing the above equations and substituting Equations (59) and (60) into Equation (58) the following equation can be obtained

$$\sum_{k=1}^{M}(\Delta_{lk}^{\mathrm{T}}+\Delta_{lk}^{\mathrm{R}})P_k'^{*}(\Omega^{*})+P_l'^{*}(\Omega^{*})/k_{\mathrm{H}l}^{*}=-z_l'^{*}(\Omega^{*}) \tag{61}$$

DOI: 10.1002/nag

The unknown item $P_l'(\Omega^*)$ can be obtained by solving Equation (61). The displacement of the ground and the rails at the exciting frequency Ω^* are given by superposition.

$$u_{\mathrm{R}}^*(x^*,\tau)=\sum_{l=1}^{M} u_{\mathrm{R}}^{\Omega}(x_t^*-a_l^*)P_l'(\Omega^*)\mathrm{e}^{i\Omega^*\tau} \tag{62}$$

$$u_z^*(x^*,\tau)=\sum_{l=1}^{M} u_z^{\Omega}(x_{\mathrm{t}}^*-a_l^*,y^*,z^*)P_l'(\Omega^*)\mathrm{e}^{i\Omega^*\tau} \tag{63}$$

3. RESULTS AND DISCUSSION

In order to demonstrate the characteristics of the response of the system, the calculations are performed for a single-axle vehicle model comprising a suspended mass M_{C} and an unsprung mass M_{W}. A detailed description of the model is given in Appendix A. Each mass has one degree of freedom in the vertical direction. The frequency of interest for the perception of ground vibration is about 5–80 Hz, and for a train speed in the range of 10–120 m/s, the corresponding wavelengths of the corrugated rail lie within the range of 0.125–24 m. The parameters for the vehicle model are listed in Table I and the parameters for the track are given in Table II, and are corresponded with those used in Sheng *et al.* [8]. The parameters of the saturated poroelastic half-space are presented in Table III, which are the same as those used by Cai *et al.* [6]. The parameters are selected according to Tables I–III if they are not denoted in the figures.

Table I. Dimensionless parameters for the single-axle vehicle model.

Suspended mass, M_{C}^*	12.9
Unsprung mass, M_{W}^*	1.173
k_{S1}^*	0.089
C_{S1}^*	0.165
$k_{\mathrm{S1}}'^*$	0.1

Table II. Dimensionless parameters for railway track.

Mass of the beam per unit length of track, m_{R}^*	0.08
Bending stiffness of the rail beam, β	0.42
Loss factor of the rail	0.01
Rail pad stiffness, k_{P}^*	11.67
Rail pad loss factor	0.15
Mass of the sleeper per unit length of the track, m_{S}^*	0.328
Mass of the ballast per unit length of the track, m_{B}^*	0.84
Ballast stiffness per unit length of the track, k_{B}^*	10.5
Loss factor of the ballast	1.0
Contact width of ballast and ground, $2L_{\mathrm{Bal}}^*$	2.7

Table III. Dimensionless parameters for fully water-saturated poroelastic soil medium.

Lamé constant, λ^*	2
Water density, ρ_{f}^*	0.53
Parameter of soil structure, m^*	1.5625
Hysteretic damping ratio, D	0.02
Ratio between the fluid viscosity and the intrinsic permeability, b^*	10
The parameter for the compressibility of the soil particle, α	0.97
The parameter for the compressibility of the fluid, M^*	12

DOI: 10.1002/nag

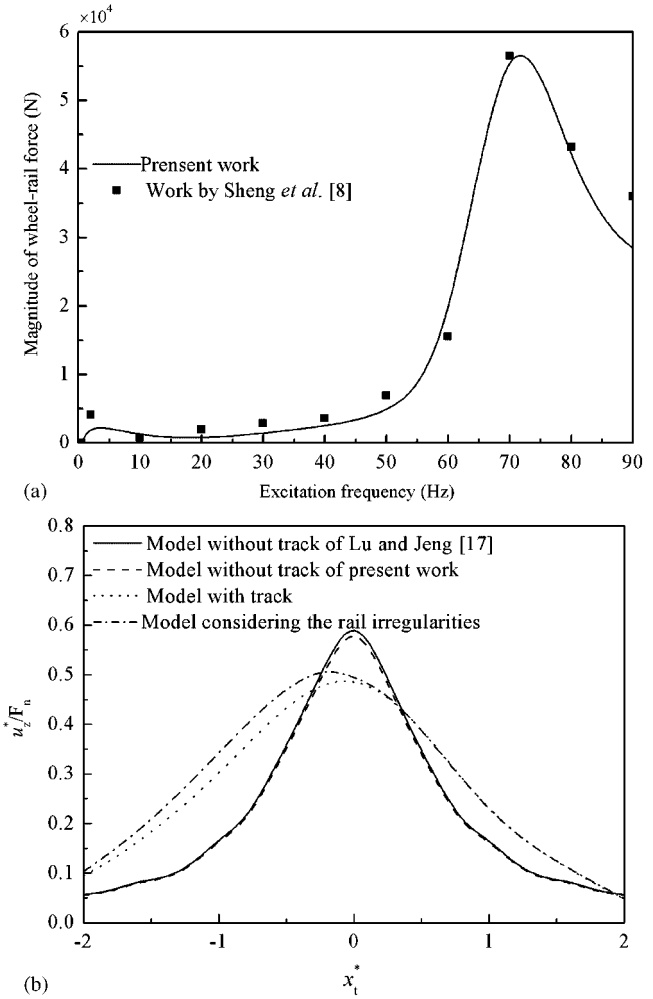

Figure 2. Comparison with existing work: (a) with that of Sheng *et al.* [8] and (b) with that of Lu and Jeng [17].

3.1. Comparison with existing work

Figure 2(a) compares the dynamic wheel–rail force for the elastic soil obtained by the present model with that obtained by Sheng *et al.* [8]. An ideal elastic half-space soil medium is simulated by choosing negligibly small values of the poroelastic parameters (ρ_f^*, b^*, M^*, and α are set to be 10^{-4}) according to Senjuntichai *et al.* [22]. The dynamic wheel–rail force is presented at the vehicle running speed of 60 m/s. It can be seen that the two results are in good agreement for the excitation frequency below 80 Hz. But as the excitation frequency increases further, the discrepancy between the two results becomes apparent. This may be due to the fact that the degeneration of poroelastic soil medium to elastic soil medium by the present method becomes inaccurate for loads with higher excitation frequency, as shown in Senjuntichai *et al.* [22].

In order to validate the algorithm of the poroelastic half-space, the track is removed and a moving point load is applied on the ground surface. The results are compared with that of Lu and Jeng [17], in which the dynamic responses of a poroelastic half-space subjected to moving point load are studied. It can be seen in Figure 2(b) that the two results are in good agreement for vehicle speed $c_0 = 0.9$. In order to investigate the effect of the track system on the ground deformation and the contribution of the dynamic load, the displacements of the ground with the track above and the displacements considering the rail irregularities are also presented in Figure 2(b). The rail irregularities are represented by a sinusoidal profile with the amplitude $A = 0.1$ mm and the

DOI: 10.1002/nag

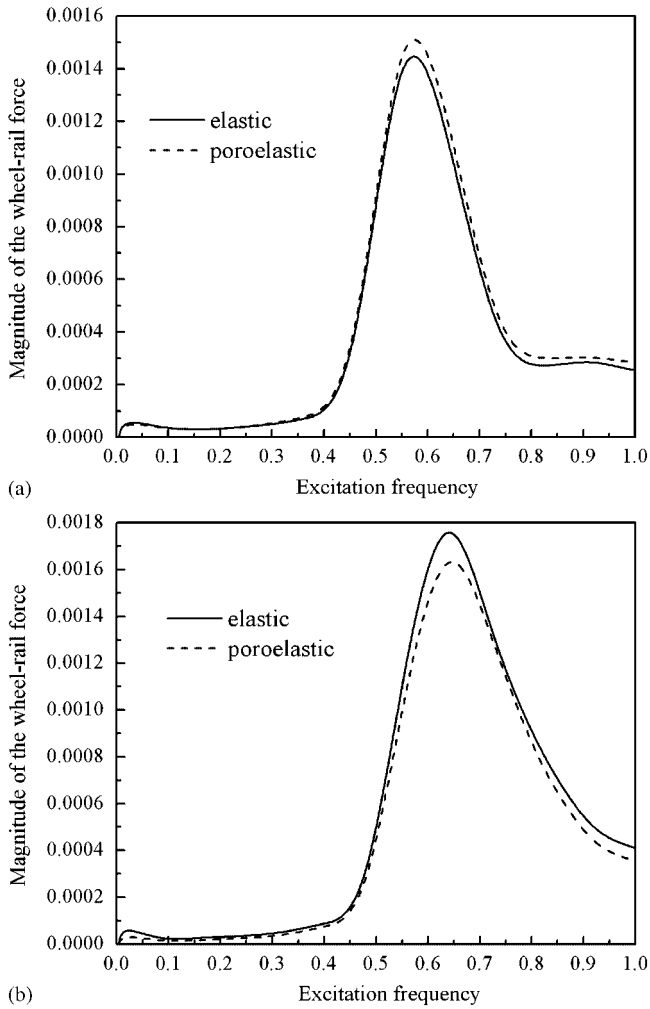

Figure 3. The magnitude of the wheel–rail forces against the excitation frequency for elastic and poroelastic soil medium: (a) $c_0 = 0.2$ and (b) $c_0 = 1.0$.

wavelength $\lambda_1 = 1.2\,\mathrm{m}$. The peak displacement of the ground with the track is smaller than that without the track, whereas the ground displacements with the track are distributed in a wider area. When considering the rail irregularities, the peak displacement increases by about 10%, and the displacement behind the load also increases apparently.

3.2. The dynamic wheel–rail force

The roughness-induced dynamic wheel–rail forces are shown in Figure 3 against the excitation frequency $f^*(f^* = c_0/\lambda_1^*)$. The dynamic wheel–rail forces for the elastic half-space soil medium are also presented for the sake of comparison. From Figure 3(a), for the case of $c_0 = 0.2$, it is shown that the shape of the two curves is very similar. The magnitude of the wheel–rail forces increases as f^* increases and reaches a maximum value at the critical frequency around $f^* = 0.55$, then decreases as f^* increases further. A close inspection of Figure 3(a), shows that the magnitude of the dynamic wheel–rail forces have a local peak at frequency 0.02, this frequency being close to the natural frequency of the suspended mass on the suspension, as noted in Sheng *et al.* [8]. The maximum wheel–rail forces for the elastic half-space is smaller than those for the poroelastic half-space at $c_0 = 0.2$. When vehicle speed increases up to $c_0 = 1.0$, as shown in Figure 3(b), the dynamic wheel–rail forces reach a maximum value at the critical frequency around $f^* = 0.65$.

DOI: 10.1002/nag

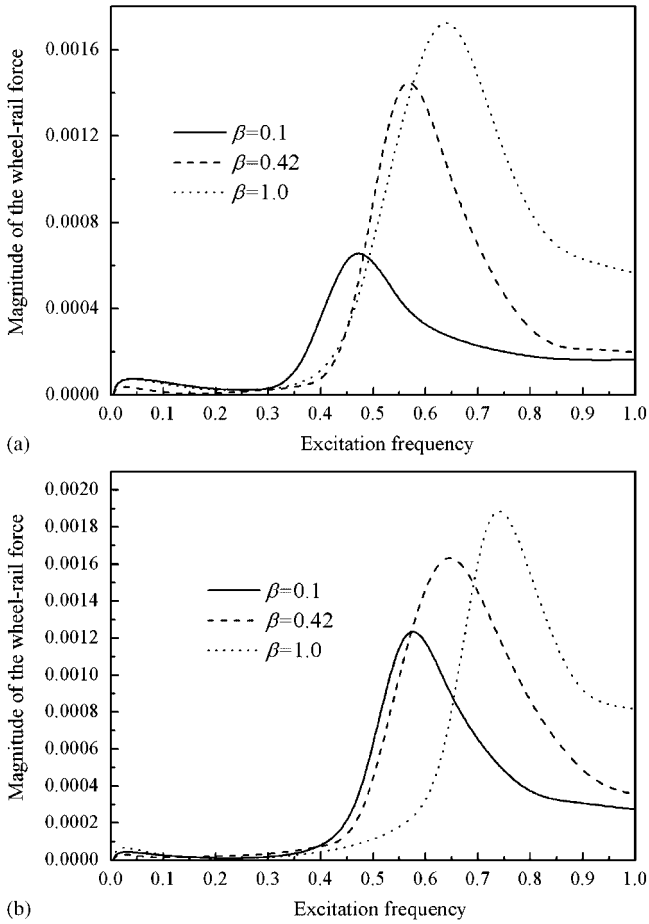

Figure 4. The magnitude of the wheel–rail forces against the excitation frequency for different β: (a) $c_0 = 0.2$ and (b) $c_0 = 1.0$.

The difference of the wheel–rail forces between the elastic half-space and the poroelastic one is more significant. The dynamic wheel–rail force for the elastic half-space is about 12% larger than that for the poroelastic half-space. This phenomenon may be explained by the results obtained by Jin [18] as follows. The receptance of the track–ground system for the elastic half-space is larger than that for the poroelastic half-space when the load speed is low, whereas it is much smaller when the load speed approaches the Rayleigh wave speed of the poroelastic half-space. The cause for this is given in Jin [18] as the dispersion of Rayleigh wave.

In Figure 4, the effects of the dimensionless bending stiffness of the rail beam (β) on the wheel–rail forces are illustrated. The maximum dynamic wheel–rail forces increase rapidly as β increases for both $c_0 = 0.2$ and $c_0 = 1.0$, and the critical frequency at which the maximum dynamic wheel–rail forces occur increases with the increase of β. When $\delta^* = 0.1$, the maximum dynamic wheel–rail forces increase by 60% as the vehicle speed varies from $c_0 = 0.2$ to $c_0 = 1.0$. For the case of $\delta = 0.42$ and $\delta = 1.0$, the vehicle speed will not change the maximum dynamic wheel–rail forces significantly.

3.3. Vertical rail displacement response

The dynamically induced rail displacements (caused by the dynamic load) are presented against excitation frequency in Figure 5. The results are given in two cases: the elastic half-space soil and the poroelastic soil. The rail beam displacements increase as f^* increases and reach a maximum value at an excitation frequency where the dynamic loads reach a maximum value. The maximum

DOI: 10.1002/nag

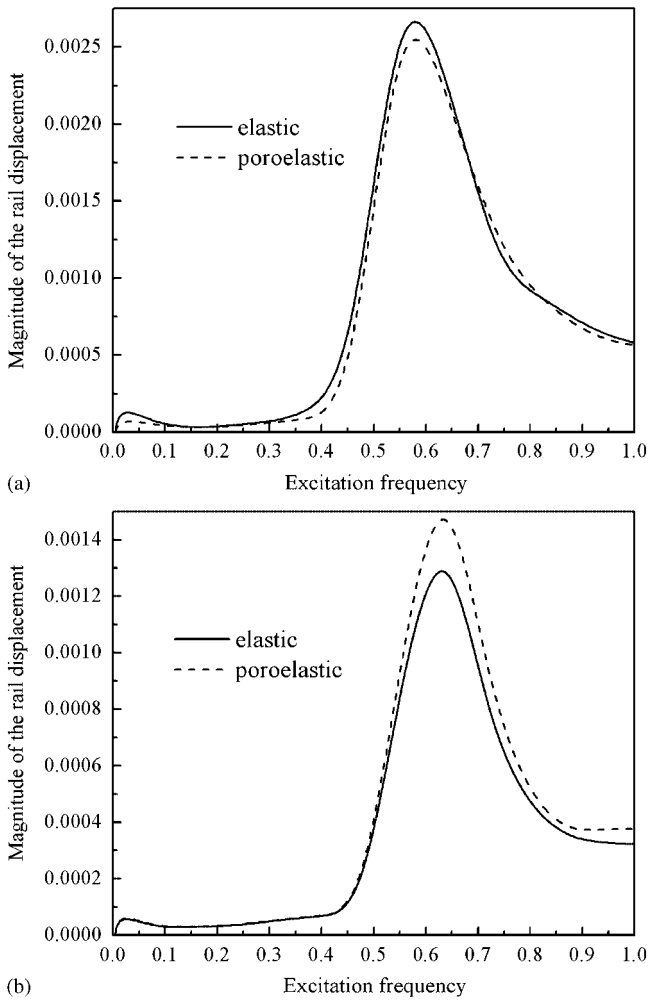

Figure 5. The magnitude of the dynamically induced rail displacement for elastic and poroelastic half-space: (a) $c_0 = 0.2$ and (b) $c_0 = 1.0$.

displacement for the elastic soil medium is slightly larger than that for the poroelastic soil medium when $c_0 = 0.2$, and 15% smaller than that for the poroelastic soil medium when $c_0 = 1.0$. However, it should be noted that the maximum dynamic load for the elastic half-space is smaller than that for the poroelastic half-space with $c_0 = 0.2$, whereas it is larger for the case of $c_0 = 1.0$ as shown in Figure 3. This phenomenon can also be explained by the dispersion of the surface wave (Rayleigh wave) of the poroelastic half-space soil medium.

For the frequency range studied in this paper, it can be obtained from Figure 5 that the maximum dynamically induced displacement occurs at the excitation frequency where the dynamic force reaches a maximum value. Thus, in order to compare the quasi-statically induced response levels (caused by axle load) with the maximum dynamically induced response levels, the results in the following paragraphs are calculated using the axle loads and the maximum dynamic loads as the inputs. The different roles of the axle loads and the maximum dynamic loads for the dynamic response of the track–ground system are identified within the vehicle speed range considered. However, it is noted that the realistic dynamically induced response levels are smaller than the presented dynamically induced response levels in most cases. The total responses are obtained as the superposition of the quasi-statically induced components and the dynamically induced ones.

The rail displacement caused by the axle load and the maximum dynamic load are presented in Figure 6, against the dimensionless vehicle speed c_0. The quasi-statically induced displacement

DOI: 10.1002/nag

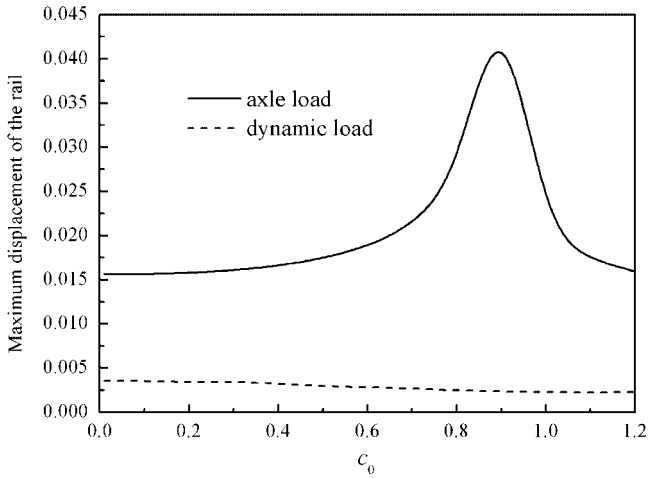

Figure 6. The maximum quasi-statically and dynamically induced rail beam displacements against c_0.

increases rapidly as c_0 increases and reaches a maximum peak at a speed of about $c_0 = 0.92$, which is close to the Rayleigh wave speed of the poroelastic half-space and is called the critical speed. It is also observed that the axle load plays a dominant role in the displacement responses of the rail beam. For the vehicle speed below $c_0 = 0.2$, the dynamically induced displacement is about 20% of the quasi-statically induced one. When the vehicle speed approaches the critical speed of the track–ground system, the quasi-statically induced displacement becomes much larger and the dynamically induced component can even be neglected. As the vehicle speed exceeds the critical speed of the track–ground system $c_0 = 1.0$, the dynamically induced displacement is about 15% of the quasi-static one.

The effect of the rail beam bending stiffness β on the rail beam displacement response is studied in Figures 7 and 8 for $c_0 = 0.2$ and $c_0 = 1.0$, respectively. The rail displacements are presented against x_t^* for three kinds of rail bending stiffnesses. In Figure 7(a), the quasi-statically induced displacements are symmetrical and reach a maximum value at the point where the load applied and the maximum displacements decrease as β increases. In Figure 7(b), the dynamically induced displacements are presented, and fluctuate apparently along the x_t^* axis. It is interesting to note that the maximum rail beam displacement caused by the dynamic loads increases as β increases. However, as the quasi-statically induced displacement component is the dominant one for the rail beam displacement, the total displacement responses of the rail beam decrease as β increases for $c_0 = 0.2$.

In Figure 8, the effect of β on the rail beam displacements for $c_0 = 1.0$ is presented. As shown in Figure 8(a), the quasi-statically induced displacements fluctuate along x_t^* and the maximum quasi-statically induced displacements decrease rapidly as β increases. In Figure 8(b), it is seen that the dynamically induced rail beam displacements fluctuate significantly along x_t^*, but the maximum displacement is much smaller than the maximum quasi-statically induced displacement, and the effect of β on the dynamically induced displacement is not apparent. As the quasi-statically induced displacements is the dominant one for the rail displacement response, it can also be concluded that increasing the rail stiffness is an efficient way for reducing the total displacement levels of the rail beam at $c_0 = 1.0$.

3.4. Accelerations of the rail beam

In Figure 9, the maximum rail beam accelerations caused by the axle load and the maximum dynamic load are presented against the dimensionless vehicle speed c_0. When the vehicle speed is low, both the quasi-statically and the dynamically induced accelerations are small. The latter accelerations are larger than the former ones and dominate the acceleration responses in this vehicle's speed range. However, the quasi-statically induced acceleration of the rail beam increases

DOI: 10.1002/nag

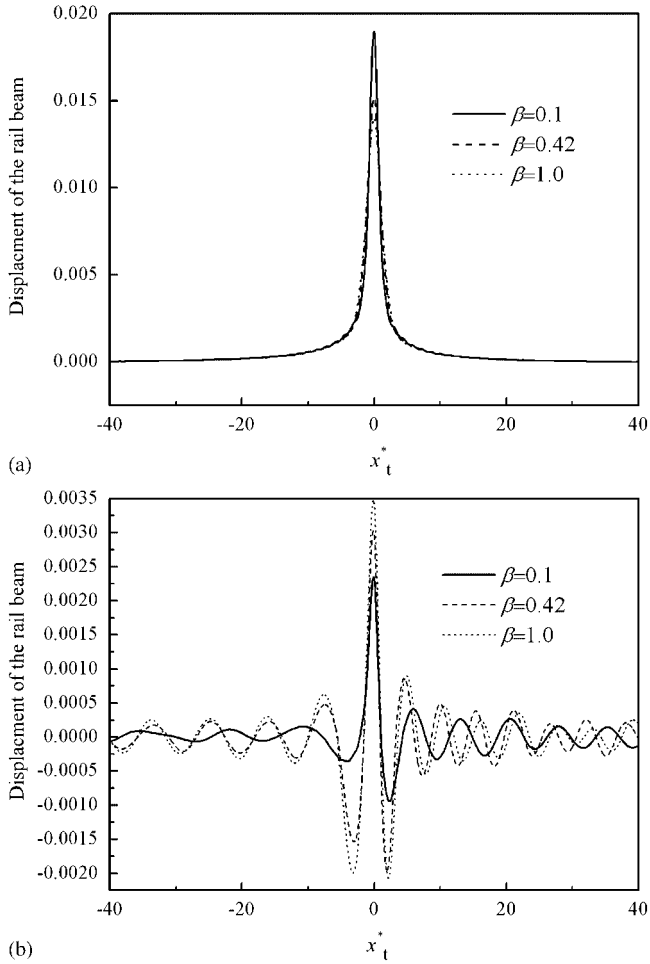

Figure 7. The rail beam displacement responses for $c_0 = 0.2$: (a) the quasi-statically induced displacements and (b) the dynamically induced displacements.

rapidly as the vehicle speed increases further and reaches the maximum value at the critical speed of the track–ground system. For the speed range around the critical speed, the quasi-statically induced accelerations are much larger than the dynamically induced ones and become the dominant ones of the rail beam acceleration response. When the vehicle speed exceeds the critical speed, the quasi-statically induced accelerations decrease with the increase of the vehicle speed. At the vehicle speed $c_0 = 1.2$, the dynamically induced acceleration component is about 25% of the quasi-statically one and cannot be neglected.

The effects of the rail beam bending stiffness β on the rail acceleration responses are studied in Figures 10–12 for $c_0 = 0.2$, $c_0 = 0.6$, and $c_0 = 1.0$, respectively. The rail acceleration responses for vehicle speed $c_0 = 0.2$ are shown in Figure 10. It is seen in Figure 10(a) that the quasi-statically induced accelerations reach a positive peak at the point where the load is applied, and the maximum accelerations of rail beam decrease as β increases. In Figure 10(b), one can see that the dynamically induced accelerations fluctuate apparently along the x_t^* axis, and their magnitude increases apparently as β increases. For vehicle speed $c_0 = 0.2$, the dynamically induced acceleration components dominate the acceleration response. It can also be concluded that the total acceleration responses of the rail beam increases with the increase of β for $c_0 = 0.2$.

Figure 11 presents the rail accelerations for the vehicle speed $c_0 = 0.6$. In Figure 11(a), it can be found that the maximum quasi-statically induced accelerations decrease apparently as β increases.

DOI: 10.1002/nag

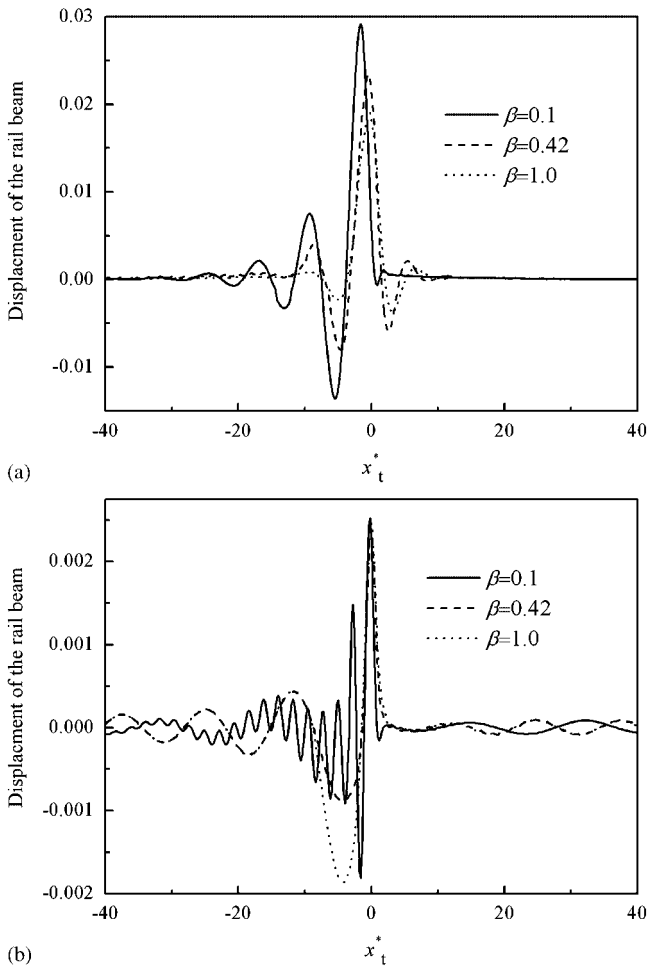

Figure 8. The rail beam displacements responses for $c_0 = 1.0$: (a) the quasi-statically induced displacements and (b) the dynamically induced displacements.

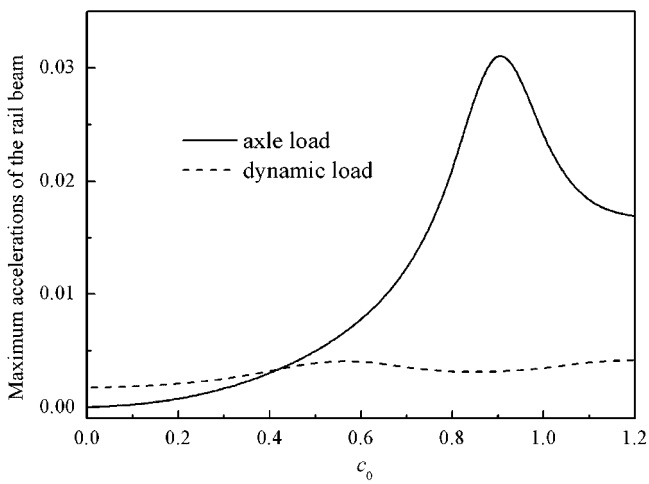

Figure 9. The maximum quasi-statically and dynamically induced rail beam accelerations against c_0.

DOI: 10.1002/nag

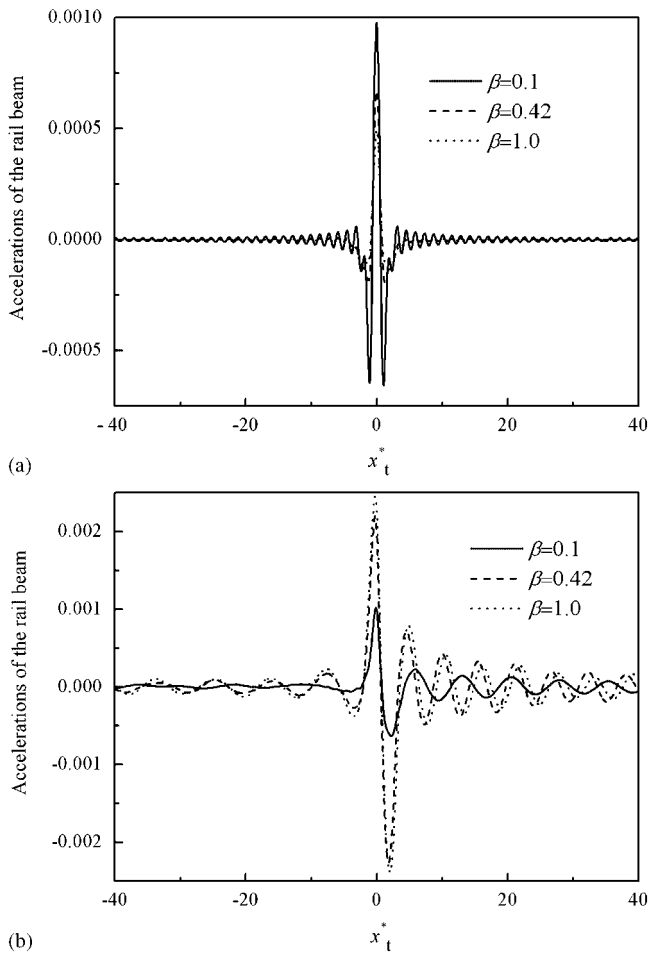

Figure 10. The rail beam accelerations for $c_0 = 0.2$: (a) the quasi-statically induced accelerations and (b) the dynamically induced accelerations.

However, for the dynamically induced components, as shown in Figure 11(b), the accelerations remain at nearly the same level as β increases. Comparing Figure 11(a) with Figure 11(b), for $\beta = 0.42$ which is close to the realistic value of the rail rigidity, the magnitude of the dynamically induced accelerations is about 60% of the quasi-statically induced accelerations. Therefore, for the vehicle speed $c_0 = 0.6$, only considering the axle load will underestimate the vibration level of the rail beam greatly. It is necessary to consider the dynamic loads for the travel's safety and comfort.

For the vehicle speed $c_0 = 1.0$, the quasi-statically induced rail accelerations fluctuate along the x_t^* axis, and the maximum acceleration response decreases rapidly with the increase of β, as shown in Figure 12(a). In Figure 12(b), the dynamically induced accelerations are much smaller than the quasi-statically induced accelerations, and the magnitude of the accelerations remains nearly the same as β increases. Therefore, for vehicle speed $c_0 = 1.0$, the quasi-statically induced vibration is the dominant one. Increasing β can reduce the total vibration level of the rail beam efficiently.

3.5. Displacement of the ground surface

In Figure 13, the maximum of ground surface displacements caused by the axle load and the dynamic load are presented for different rail stiffnesses at $y^* = 0$ against the dimensionless vehicle speed sc_0. The curve for the ground surface displacement is similar to that for the rail beam displacement. The quasi-statically induced displacement component dominates the

DOI: 10.1002/nag

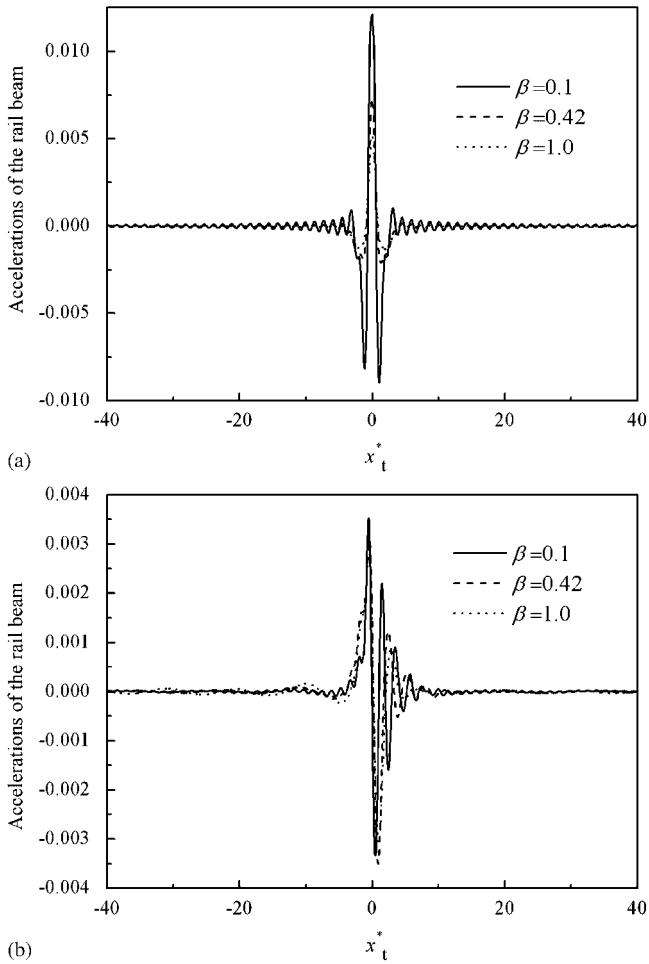

Figure 11. The rail beam accelerations for $c_0 = 0.6$: (a) the quasi-statically induced accelerations and (b) the dynamically induced accelerations.

ground surface displacement responses and reaches the maximum value at the critical speed of the track–ground system. The dynamically induced displacement is about 20% of the quasi-statically induced when the vehicle speed is low. At the critical speed of the track–ground system, the quasi-statically induced ground surface displacement is much larger than the dynamically induced. It can be seen that the effects of β are apparent on the quasi-statically induced ground surface displacement. The quasi-statically induced displacement decreases rapidly as β increases. However, the effects of β on the dynamically induced ground displacement are not so obvious.

3.6. Accelerations of the ground surface

In Figure 14, the effects of β on the magnitude of the ground surface accelerations at $y^* = 0$ are studied. When the vehicle speed is low, the accelerations caused by both the axle load and dynamic load are small, and the dynamically induced accelerations are larger than the quasi-statically induced. The dynamically induced accelerations are the dominant ones for the low-vehicle-speed condition. As the vehicle speed increases further, the quasi-statically induced ground accelerations increase rapidly and become the dominant source of the ground acceleration response. The effect of β on the ground surface accelerations is not apparent when the vehicle speed is low. It can also be

DOI: 10.1002/nag

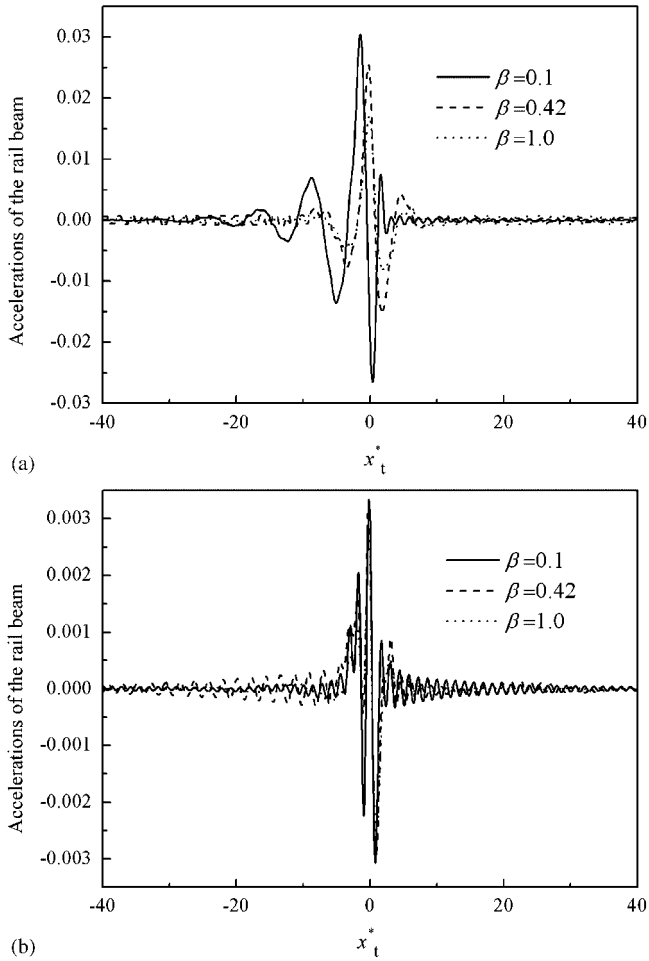

Figure 12. The rail beam accelerations for $c_0 = 1.0$: (a) the quasi-statically induced accelerations and (b) the dynamically induced accelerations.

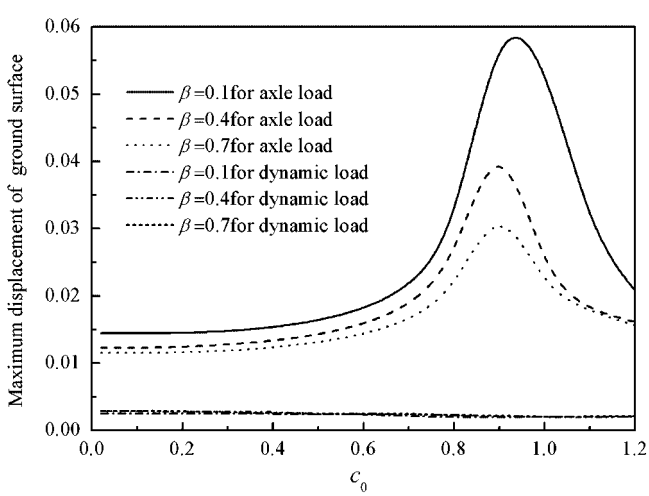

Figure 13. The maximum quasi-statically and dynamically induced ground surface displacements against c_0.

DOI: 10.1002/nag

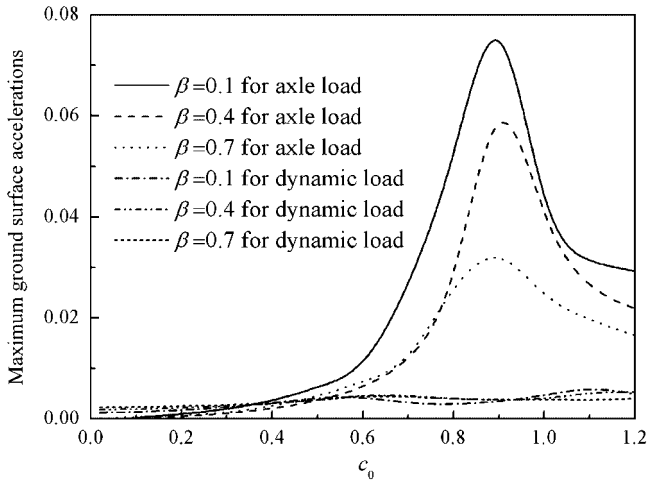

Figure 14. The maximum quasi-statically and dynamically induced ground surface accelerations against c_0.

seen that the dynamically induced accelerations increase as β increases, whereas the quasi-statically induced acceleration decreases with the increase of β. The total vibration levels increase with the increase of β. As the vehicle speed approaches the Rayleigh wave speed of the half-space, the quasi-statically induced accelerations are much larger, and decrease rapidly with the increase of β. The effect of β on the dynamically induced accelerations is not apparent. For this vehicle speed range, the total vibration level decreases rapidly as β increases. Comparing Figure 14 with Figure 9, it can also be found that the acceleration response level of the ground surface at $y^*=0$ is smaller than that for the rail beam when the vehicle speed is low, whereas it is larger when the vehicle speed approaches the Rayleigh wave speed.

In order to study the attenuation of the ground vibration, the magnitude of accelerations for both axle and dynamic loads are presented against y^* in Figure 15. In Figure 15(a), when $c_0=0.2$, the quasi-statically induced acceleration decreases rapidly as y^* increases, nearly zero at $y^*=5$. The dynamically induced acceleration is much larger at $y^*=0$ and decreases more slowly. The dynamically-induced component of vibration is the dominant one for the acceleration response of the free field. In Figure 15(a), the acceleration response for the elastic half-space soil medium is also presented. It can be seen that the acceleration responses predicted by the elastic soil model is larger than that by the poroelastic soil model for both axle and dynamic loads at $y^*=0$, and the acceleration responses attenuate more slowly in the elastic soil medium. The free-field acceleration response predicted by elastic soil model is larger than that by the poroelastic one. In Figure 15(b), when $c_0=0.6$, the quasi-statically induced acceleration is larger than the dynamically induced acceleration at $y^*=0$, but the dynamically induced vibration component dissipates more slowly and gives rise to the majority of the vibrations for the free field off the track. For the case of the elastic soil medium, it can be seen that the acceleration response dissipates more slowly in the elastic soil. Using the elastic soil medium model will overestimate the acceleration response under the free-field condition for $c_0=0.6$. In Figure 15(c), for $c_0=1.0$, the quasi-statically induced accelerations are much larger and are the dominant components for the ground vibration at various y^*. The acceleration response predicted by the elastic soil model is apparently smaller than that by the poroelastic soil model.

Therefore, for vehicle speed below the Rayleigh wave speed, the free-field acceleration response is dominated by the dynamic load. But when the vehicle speed approaches the Rayleigh wave speed of the half-space, the axle load is the dominant one for the acceleration response of the free field. Using the elastic soil medium model will overestimate the acceleration response level of the free field for the train speed below Rayleigh wave speed whereas it will underestimate the response level for the train speed above the Rayleigh wave speed.

DOI: 10.1002/nag

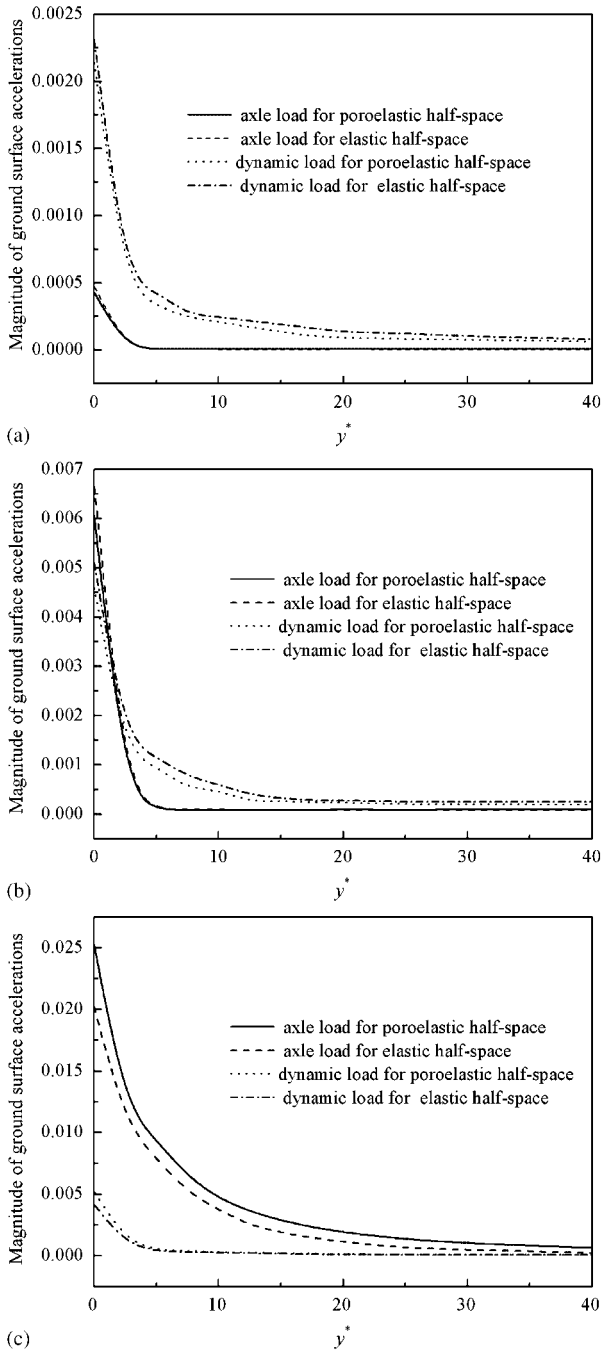

Figure 15. The quasi-statically and dynamically induced accelerations of the ground surface against y^*: (a) $c_0 = 0.2$, (b) $c_0 = 0.6$, and (c) $c_0 = 1.0$.

3.7. Excess pore water pressure of the ground

In Figure 16, the train-induced excess pore water pressures are studied. In Figure 16(a), when $c_0 = 0.2$, the quasi-statically induced pore water pressure reaches a positive peak at the load point and a negative peak behind the load. The dynamically induced pore water pressure fluctuates along x_t^* and the maximum value is larger than that by the quasi-statically induced one. When the vehicle speed exceeds the critical speed, as shown in Figure 16(b), the quasi-statically induced pore water pressure becomes much larger and is the dominant component for the pore water pressure responses.

DOI: 10.1002/nag

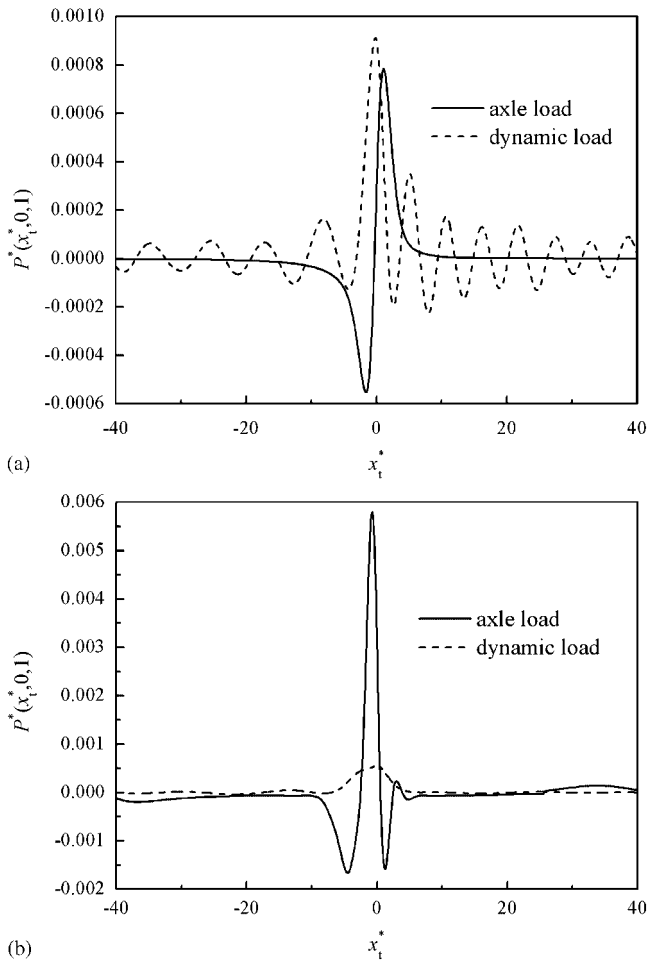

Figure 16. The quasi-statically and dynamically induced pore water pressures: (a) $c_0 = 0.2$ and (b) $c_0 = 1.0$.

4. CONCLUSIONS

In this paper, the dynamic responses of track–ground system subjected to the moving train loads are investigated using a vehicle–track–ground coupling model. The governing equations are solved by Fourier transform and the time domain results are calculated by fast inverse Fourier transform. The effects of vehicle speed and rail stiffness on the dynamic responses of the track–ground system are studied, and the different characteristics of the elastic soil medium and the poroelastic one subjected to a moving train load are investigated. In addition, the different roles of the axle load and dynamic wheel–rail load for the dynamic responses of the track–ground system are identified for vehicle speeds below and above the Rayleigh wave speed. The main conclusions of this study can be summarized as follows:

1. The total displacement responses of the rail and ground are dominated by quasi-statically induced displacement components for various vehicle speeds, and the total displacement response levels become much larger as the vehicle speed reaches the critical speed. The quasi-statically induced displacements decrease rapidly as β increases, whereas the dynamically induced displacement remains at nearly the same level with the increase of β. Thus, increasing the rail stiffness is still an efficient way of reducing the total displacements of the rail and the ground, especially when the vehicle speed approaches the Rayleigh wave speed of the half-space.

DOI: 10.1002/nag

2. The quasi-statically induced and the dynamically induced rail beam accelerations are small when the vehicle speed is slow, but the dynamically induced accelerations dominate the rail beam acceleration responses for this vehicle speed range. As the vehicle speed increases, the quasi-statically induced acceleration increases rapidly and becomes the dominant one when the vehicle speed approaches the critical speed, however, the dynamically induced acceleration still cannot be neglected. The increase of the rail stiffness can reduce the total vibration level efficiently for the vehicle speed around the Rayleigh wave speed of the half-space.
3. For vehicle speed below the critical speed, the dynamically induced ground surface accelerations give rise to the majority of the ground acceleration responses, and are the dominant components for the ground vibration of the free field. As the vehicle speed exceeds the critical speed, the quasi-statically induced ground surface accelerations are much larger and dissipate more slowly in the ground, becoming the dominant one for the acceleration responses of the free field. It is found that the total acceleration responses of the free field predicted by the elastic soil model are larger than those predicted by the saturated poroelastic soil model at the vehicle speed below the critical speed, while are considerably smaller at the vehicle speed above the critical speed.
4. For vehicle speed below the critical speed, the dynamically induced excess pore water pressure is larger than the quasi-statically induced one. As the vehicle speed exceeds the Rayleigh wave speed of the poroelastic half-space, the quasi-statically induced pore water pressure is much larger than the dynamically induced one and is the dominant one for the excess pore water pressure response.

APPENDIX A

The details and parameters of the vehicle are shown in Figure A1. The displacement vector of the vehicle is defined as

$$\mathbf{Z_V}(t)=(Z_C(t), \varphi_C(t), Z_{B1}(t), \varphi_{B1}(t), Z_{B2}(t), \varphi_{B2}(t), Z_{W1}(t), Z_{W2}(t), Z_{W3}(t), Z_{W4}(t)) \tag{A1}$$

Corresponding to this displacement vector, the external load vector is determined as

$$\mathbf{F_V}(t)=(0,0,0,0,0,0,-P_1(t),-P_2(t),-P_3(t),-P_4(t))^T=-\mathbf{BP}(t) \tag{A2}$$

where

$$\mathbf{B}=\begin{bmatrix}\mathbf{0}_{6\times4}\\ \mathbf{I}_{4\times4}\end{bmatrix} \tag{A3}$$

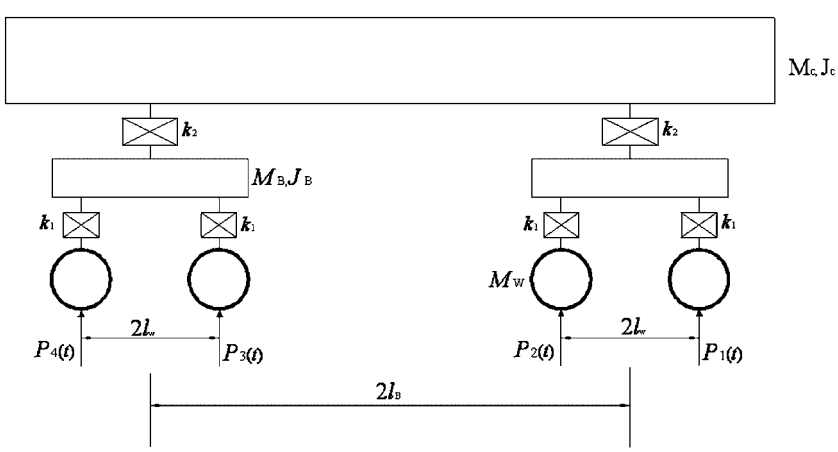

Figure A1. The details of the vehicle model.

DOI: 10.1002/nag

and

$$\mathbf{P}(t)=(P_1(t), P_2(t), P_3(t), P_4(t))^{\mathrm{T}} \tag{A4}$$

is the vertical wheel–rail load vector.

The wheelset displacement vector can be written as

$$\mathbf{Z_W}(t)=\mathbf{A}\mathbf{Z_V}(t) \tag{A5}$$

where

$$\mathbf{A}=[\mathbf{0}_{4\times 6}\ \ \mathbf{I}_{4\times 4}]=\mathbf{B}^{\mathrm{T}}. \tag{A6}$$

The mass matrix is given by

$$\mathbf{M_V}=\mathrm{diag}(M_{\mathrm{C}}, J_{\mathrm{C}}, M_{\mathrm{B}}, J_{\mathrm{B}}, M_{\mathrm{B}}, J_{\mathrm{B}}, M_{\mathrm{W}}, M_{\mathrm{W}}, M_{\mathrm{W}}, M_{\mathrm{W}}) \tag{A7}$$

The stiffness matrix is given by

$$\mathbf{K_V}=\begin{bmatrix} 2k_2 & 0 & -k_2 & 0 & -k_2 & 0 & 0 & 0 & 0 & 0 \\ 0 & 2k_2 l_{\mathrm{B}}^2 & -k_2 l_{\mathrm{B}} & 0 & k_2 l_{\mathrm{B}} & 0 & 0 & 0 & 0 & 0 \\ -k_2 & -k_2 l_{\mathrm{B}} & k_2+2k_1 & 0 & 0 & 0 & -k_1 & -k_1 & 0 & 0 \\ 0 & 0 & 0 & 2k_1 l_{\mathrm{W}}^2 & 0 & 0 & -k_1 l_{\mathrm{w}} & k_1 l_{\mathrm{w}} & 0 & 0 \\ -k_2 & k_2 l_{\mathrm{B}} & 0 & 0 & k_2+2k_1 & 0 & 0 & 0 & -k_1 & -k_1 \\ 0 & 0 & 0 & 0 & 0 & 2k_1 l_{\mathrm{W}}^2 & 0 & 0 & -k_1 l_{\mathrm{w}} & k_1 l_{\mathrm{w}} \\ 0 & 0 & -k_1 & -k_1 l_{\mathrm{w}} & 0 & 0 & k_1 & 0 & 0 & 0 \\ 0 & 0 & -k_1 & k_1 l_{\mathrm{w}} & 0 & 0 & 0 & k_1 & 0 & 0 \\ 0 & 0 & 0 & 0 & -k_1 & -k_1 l_{\mathrm{w}} & 0 & 0 & k_1 & 0 \\ 0 & 0 & 0 & 0 & -k_1 & k_1 l_{\mathrm{w}} & 0 & 0 & 0 & k_1 \end{bmatrix} \tag{A8}$$

The single axle vehicle model and the structure of suspensions are shown in Figure A2

$$k_1=\frac{k_{\mathrm{S1}}k'_{\mathrm{S1}}+i\Omega c_{\mathrm{S1}}(k_{\mathrm{S1}}+k'_{\mathrm{S1}})}{k'_{\mathrm{S1}}+i\Omega c_{\mathrm{S1}}} \tag{A9}$$

The hysteretic damping can be incorporated into the suspension by introducing a complex spring stiffness.

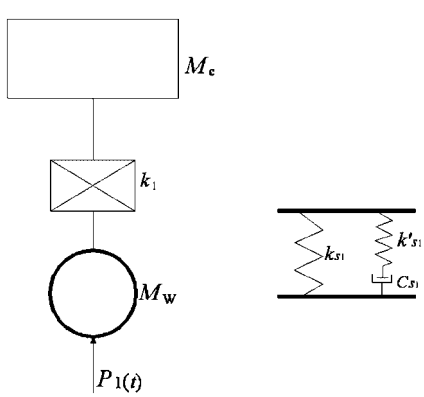

Figure A2. The single axle model and the structure of suspensions.

DOI: 10.1002/nag

Then, the receptance of the wheel at the wheel–rail contact point Δ_{11}^{T} is given by

$$\Delta_{11}^{\mathrm{T}} = \frac{k_1 - M_{\mathrm{C}}\Omega^2}{M_{\mathrm{C}}M_{\mathrm{W}}\Omega^4 - k_1 M_{\mathrm{C}}\Omega^2 - k_1 M_{\mathrm{W}}\Omega^2} \tag{A10}$$

ACKNOWLEDGEMENTS

The work presented in this paper is supported by the National Natural Science Foundation of China (Grant No. 50778136), the Provincial Natural Science Foundation of Zhejiang (Grant No. R1080819), and the China Postdoctoral Science Foundation (Grant No. 20090450182).

REFERENCES

1. Krylov V. Generation of ground vibrations by superfast trains. *Applied Acoustics* 1995; **44**:149–164.
2. Vostroukhov AV, Metrikine AV. Periodically supported beam on a visco-elastic layer as a model for dynamic analysis of a high-speed railway track. *Soil Dynamics and Earthquake Engineering* 2003; **40**:5723–5752.
3. Takemiya H, Bian X. Substructure simulation of inhomogeneous track and layered ground dynamic interaction under train passage. *Journal of Engineering Mechanics* (ASCE) 2005; **131**(7):699–711.
4. Sheng X, Jones CJC. Ground vibration generated by a harmonic load acting on a railway track. *Journal of Sound and Vibration* 1999; **225**(1):3–28.
5. Picoux B, Le Houédec D. Diagnosis and prediction of vibration from railway trains. *Soil Dynamics and Earthquake Engineering* 2005; **25**:905–921.
6. Cai Y, Sun H, Xu C. Response of railway track system on poroelastic half-space soil medium subjected to a moving train load. *International Journal of Solids and Structures* 2008; **45**:5015–5034.
7. Lai CG, Callerio A, Faccioli E. Mathematical modeling of railway-induced ground vibrations. *Proceedings of the International Workshop Wave 2000*, Bochum, Germany, 2000; 99–110.
8. Sheng X, Jones CJC, Thompson DJ. A theoretical model for ground vibration from trains generated by the vertical track irregularities. *Journal of Sound and Vibration* 2004; **272**:937–965.
9. Zai W, Cai Z. Dynamic interaction between a lumped mass vehicle and a discretely supported continuous rail track. *Computers and Structures* 1997; **63**(5):987–997.
10. Sun Y, Dhanasekar M. Dynamic model for the vehicle interactions of the rail track and wagon system. *International Journal of Solids and Structures* 2002; **39**:1337–1359.
11. Jenkins HH, Stephenson JE, Clayton GA, Morland GW, Lyon D. The effect of track and vehicle parameters on wheel/rail vertical dynamic loads. *Rail Engineering Journal* 1974; **3**(1):2–16.
12. Biot MA. Theory of propagation of elastic waves in a fluid-saturated porous solid. Part I: Low-frequency range; part II: high-frequency range. *Journal of the Acoustical Society of America* 1956; **28**:168–191.
13. Biot MA. Mechanics of deformation and acoustic propagation in porous media. *Journal of Applied Physics* 1962; **33**:1482–1498.
14. Siddharthan R, Zafir Z, Norris GM. Moving load response of layered soil. I: Formulation; II: verification and application. *Journal of Engineering Mechanics* (ASCE) 1993; **119**(10):2052–2089.
15. Theodorakopoulos DD. Dynamic analysis of a poroelastic half-space soil medium under moving loads. *Soil Dynamics and Earthquake Engineering* 2003; **23**:521–533.
16. Theodorakopoulos DD, Chassiakoos AP. Dynamic effects of moving load on poroelastic soil medium by an approximate method. *International Journal of Solids and Structures* 2004; **41**:1801–1822.
17. Lu JF, Jeng DS. A half-space saturated poro-elastic medium subjected to a moving point load. *International Journal of Solids and Structures* 2007; **44**:573–586.
18. Jin B. Dynamic response of a poroelastic half space generated by high speed load. *Chinese Quarterly of Mechanics* (*in Chinese*) 2004; **25**:168–174.
19. Knothe K, Grassie SL. Modelling of railway track and vehicle track interaction at high frequencies. *Vehicle System Dynamics* 1993; **22**:209–262.
20. Grassie SL, Gregory RW, Harrison D, Johnson KL. The dynamic response of railway track to high frequency vertical excitation. *Journal of Mechanical Engineering Science* 1982; **24**(2):77–90.
21. Suiker ASJ, Chang CS, De Borst R, Esveld C. Surface waves in a stratified half space with enhanced continuum properties. Part 1: Formulation of the boundary value problem. *European Journal of Mechanics A*: *Solids* 1999; **18**:749–768.
22. Senjuntichai T, Mani S, Rajapakse RKND. Vertical vibration of an embedded rigid foundation in a poroelastic soil. *Soil Dynamics and Earthquake Engineering* 2006; **26**:626–636.